Label-Free Measurement of Cell–Electrode Cleft Gap Distance with High Spatial Resolution Surface Plasmon Microscopy

Koji Toma,[*,†,§] Hiroshi Kano,[‡] and Andreas Offenhäusser[†]

[†]Institute of Bioelectronics (ICS-8/PGI-8), Forschungszentrum Jülich GmbH, 52425 Jülich, Germany and [‡]Division of Information and Electronic Engineering, Graduate School of Engineering, Muroran Institute of Technology, Hokkaido 0508585, Japan. [§]Present address: Department of Biomedical Devices and Instrumentation, Institute of Biomaterials and Bioengineering, Tokyo Medical and Dental University, Tokyo 1010062, Japan.

ABSTRACT Understanding the interface between cells or tissues and artificial materials is of critical importance for a broad range of areas. For example, in neurotechnology, the interfaces between neurons and external devices create a link between technical and the nervous systems by stimulating or recording from neural tissue. Here, a more effective interface is required to enhance the electrical characteristics of neuronal recordings and stimulations. Up to now, the lack of a systematic characterization of cell–electrode interaction turns out to be the major bottleneck. In this work, we employed a recently developed surface plasmon microscope (SPM) to monitor in real-time the cell–metal interface and to measure *in situ* the gap distance of the cleft with the spatial resolution reaching to the optical diffraction limit. The SPM allowed determination of the distance of human embryonic kidney 293 cells cultured on gold surfaces coated with various peptides or proteins without any labeling. This method can dramatically simplify the interaction investigation at metal–living cell interface and should be incorporated into systematic characterization methods.

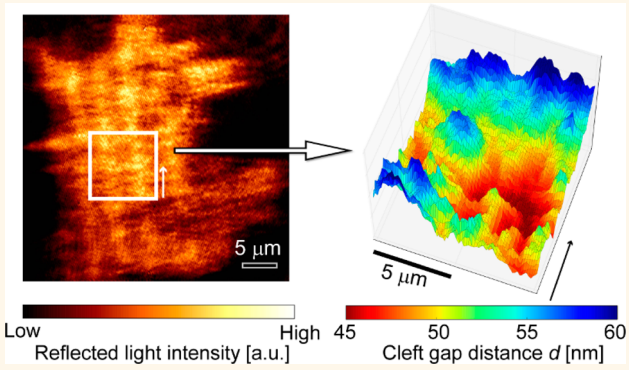

KEYWORDS: surface plasmon microscopy · label-free · real-time · biointerface · cell–electrode gap distance

The rise of modern technology in biology and medicine has drastically increased the importance of the bio-interface. In fundamental neuroscience and biomedical research, for extracellular recording, the electric signal at the membrane surface is measured noninvasively, incurring less damage to a cell and thus longer recording times. Despite these features, the recorded signals are about 2 orders of magnitude lower than those measured with intracellular recording.[1] The signal intensity is largely determined by cell–electrode geometry, for example, the relative positions of the cell and electrode. Therefore, to date, in conjunction with various adhesion promotion techniques including chemical or biological modifications[2,3] and nanostructuring,[4–6] the characterization and analysis of the cell–electrode interface have become very important. Widely used techniques for observation of the interface include reflection interference contrast microscopy (RICM),[7,8] total internal reflection fluorescence (TIRF) microscopy,[9] fluorescence interference contrast (FLIC) microscopy,[3,10–12] transmission electron microscopy (TEM),[13–16] and scanning electron microscopy (SEM).[6,17–20] Recently, a technique using metal-induced energy transfer has also been introduced.[21] For TIRF and FLIC microscopy, the interfacing membrane is stained with fluorophores. Due to the intrinsic high light intensity of fluorophores, such fluorescence microscopy enables acquisition of images with clear contrast. In addition, it offers an excellent axial resolution. In particular, FLIC microscopy is capable of resolving 1 nm differences in depth.[11] However, additional staining process, possible inhomogeneous binding of

* Address correspondence to toma.bdi@tmd.ac.jp.

Received for review September 29, 2014 and accepted November 25, 2014.

Published online November 25, 2014
10.1021/nn505521e

fluorophores to the region of interest, and photobleaching make quantitative analysis difficult. For TEM and SEM, although sub-nanometer spatial resolution can be attained,[13] complicated and time-consuming pretreatments, such as fixation, dehydration, and cutting by focused ion beam for cross-section observation, are required to observe cells in vacuum. Furthermore, the risk of artifacts due to pretreatment cannot be neglected. Therefore, for TEM and SEM, real-time monitoring of the cell–electrode interface is very challenging.

Surface plasmon microscope (SPM) was introduced in order to image low-contrast samples,[22,23] for example, a Langmuir–Blodgett film[24] without labeling. It exploits surface plasmon polaritons (SPPs), electromagnetic waves propagating along a metal–dielectric interface, and allowed real-time investigation of the interface. SPM was also employed to observe cells, especially their interfaces with substrates.[25−28] Despite these advantages, its spatial resolution is considered to be an issue due to the propagating property of SPPs at the interface. The spatial resolution is limited by the propagation length of SPPs, which for gold is typically about 7 μm at 633 nm wavelength.[29] In order to break through the spatial resolution barrier, some works have been reported, including wide-field, Bragg-scattered SPPs and localized SPPs.[29−34] Especially in localized SPPs, excitation light is tightly focused at a metal thin film through a high numerical aperture microscope objective. A fraction of the wavenumber of the light matches to the propagation constant of SPPs, giving rise to SPPs. Finally, the excited coherent SPPs constructively interfere at the center, leading to the localization of SPPs and enabling one to achieve high spatial resolution up to the optical diffraction limit (approximately 210 nm with a gold film in air at 632.8 nm wavelength).[35] The aforementioned standard SPM with the Kretschmann configuration was also realized by using a high numerical aperture microscope objective, where an excitation light is made incident at an angle to match the resonant condition by focusing the light at a back focal plane (BFP) of the microscope objective.[36,37] Recently, a new SPM combining these two microscopies, one with the standard Kretschmann configuration (lens-imaging-type SPM, LISPM) and the other with localized SPPs (scanning localized SPM, SLSPM), was introduced.[38] It takes advantages of LISPM with simultaneous large area observation and SLSPM with the high spatial resolution.

Here we employ this combined SPM for label-free measurement of the cell–electrode cleft gap distance. In the experiments, human embryonic kidney (HEK) 293 cells are chosen since they are relatively easy to treat and their biointerface has been well studied with other microscopy techiques, thereby being used to validate our approach. Owing to the advantages of SPPs, the setup allows *in situ* and real-time observation of the cell–gold interface, by which one can select the region of interest for the gap measurement. By scanning the area with SLSPM, the gap distance with various adhesion proteins and peptides are quantitatively determined. In addition, high spatial resolution of SLSPM enables one to observe the morphology of the cellular bottom membrane in detail, which is difficult in the conventional SPM (*i.e.*, LISPM). Compared with other conventional microscopy, our approach benefits from the label-free and *in situ* measurement of the gap distance in high spatial resolution, thereby becoming a simple and accurate surface characterization technique.

RESULTS AND DISCUSSION

Combined SPM Construction. The combined SPM setup was constructed based on the previous work and is depicted in Figure 1.[38] Employing flipping mirrors, it is able to switch the microscope. Briefly, in LISPM, a linearly polarized light at 632.8 nm wavelength is expanded and then focused with a lens (L4) at BFP of a microscope objective at an offset from the optical axis. It gives rise to a plane wave incident to the substrate at a high enough incident angle θ_{ex} to meet the excitation condition of SPPs as also described in the work of Huang *et al.*[36] or Halpern *et al.*[37] In SLSPM, the polarization of the expanded light is changed from the linear to the radial. It improves the spatial resolution of SLSPM because in the radial a normal component of the electric field E_z to a surface (z-coordinate in Figure 1), which approximately represents the distribution of SPPs, is enhanced by constructive interference at the focus, while in the linear, it is canceled by destructive interference. For example, with a gold in air at 632.8 nm wavelength, the electric field intensity $|E_z|^2$ distribution has one peak with the full width at half-maximum of 210 nm, in contrast to two peaks with the distance of 330 nm for the linear.[35] The radial polarized light is then relayed with two lenses (L1 and L2) to BFP and is tightly focused on the substrate with the microscope objective. The BFP is imaged at each scanning step over an area of interest.

Real-Time Imaging of HEK293 Cell–Gold Interface with LISPM. First, the imaging properties of LISPM were assessed. In this experiment, HEK293 cells were cultured on poly-L-lysine (PLL)-coated gold surfaces for 3 days *in vitro* (DIV). As the control, the cells were cultured on bare gold surfaces. The images taken with differential interference contrast (DIC) microscope and LISPM are presented in Figure 2. The images with a DIC microscope show the differences in morphologies of the cells cultured on the PLL-coated and bare surfaces (Figure 2a,b). The cells on the PLL-coated stretch their body, implying high adhesion, while those on the bare are rounded, indicating relatively low adhesion. However, one cannot give a direct conclusion to adhesion from these images since through DIC the interfacial information is hidden.

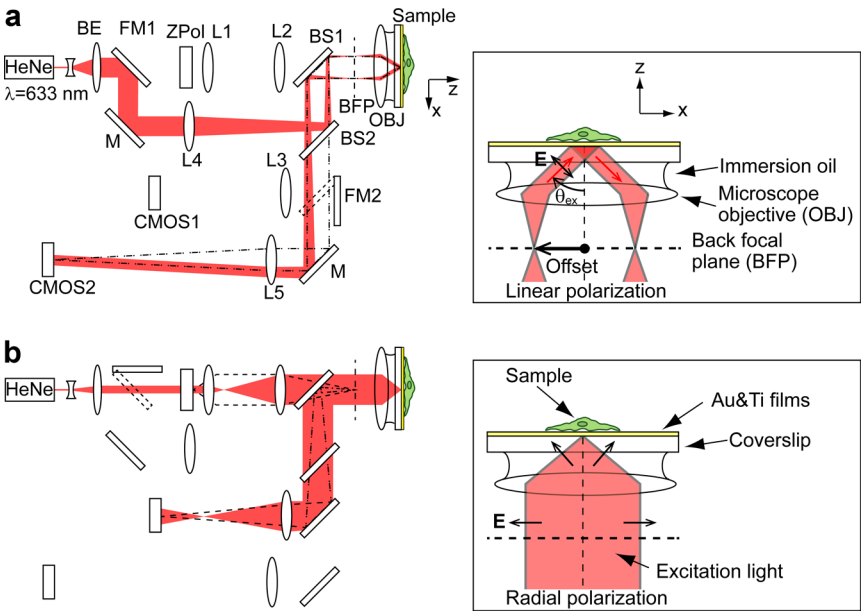

Figure 1. Schematic drawings of the combined SPM setup for (a) LISPM and (b) SLSPM. The insets show the detailed optical path of the light nearby the sample. The microscope is switchable by flipping mirrors (FM1 and FM2). BE, beam expander; FM, flipping mirror; L, lens; BS, beam splitter; M, mirror; OBJ, microscope objective; BFP, back focal plane of OBJ.

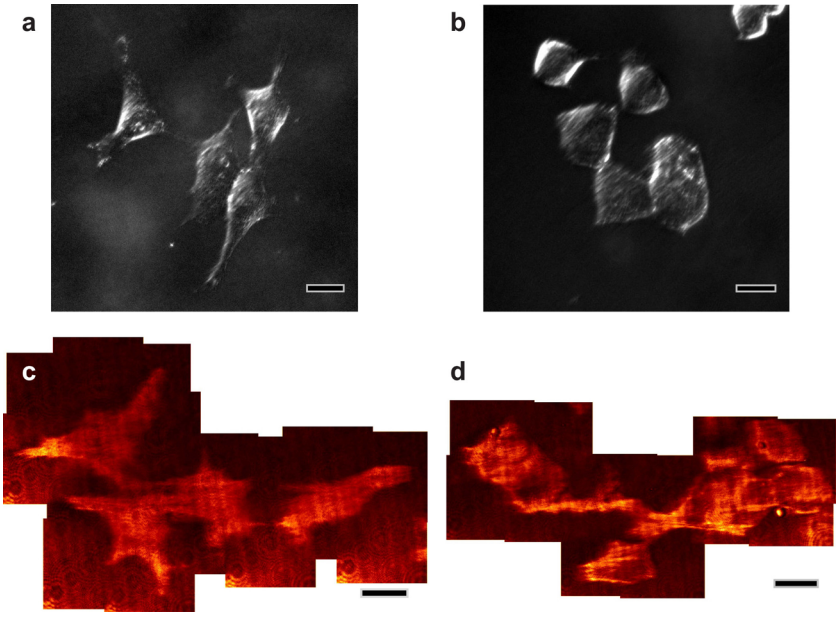

Figure 2. Comparison of DIC microscope and LISPM images. (a,b) Images of HEK293 cells grown on PLL-coated and (left column) bare gold (right column) surfaces taken with DIC microscope. (c,d) Those taken with LISPM. Note that the cells are on the same substrate for each surface coating but are not identical. Scale bars are 20 μm.

To elucidate the interface, the observation with LISPM was carried out, and the results are presented in Figure 2c,d. Let us note that those cells shown in Figure 2a,c and Figure 2b,d were cultured on the same substrate but were not identical. During this experiment, the incident angle of the light was set at the surface plasmon resonance (SPR) angle for the region without the cells (dark part in the picture). Although LISPM provides only cell−gold interface information, the images show cell shapes similar to those observed with DIC microscopy. Furthermore, the strength of the cell adhesion on the substrates is visualized as reflected light intensity contrast; that is, the brighter the area is, the better the cell adheres to the substrate. LISPM images of the cells on the bare surface show inhomogeneous cell adhesion and dark areas at the cell center, while the cells on the PLL-coated substrates show homogeneous and good adhesion. This indicates that cells on the PLL-coated adhere better to the substrate than those on the bare substrate.

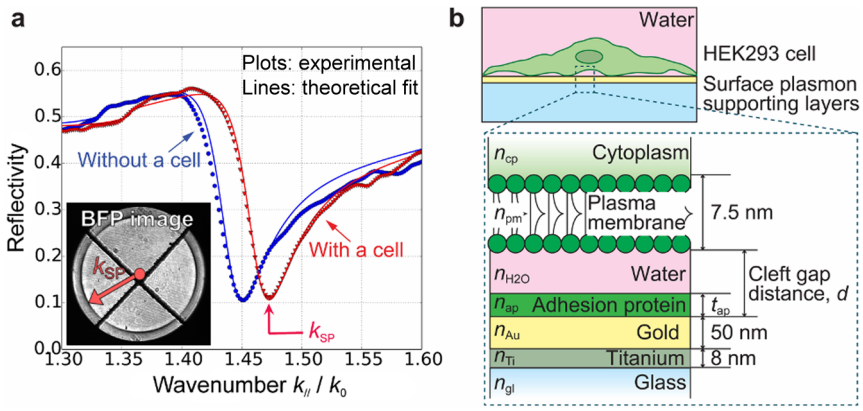

Figure 3. (a) Reflectivity spectra as a function of the in-plane wavenumber $k_{//}$ normalized with that in vacuum k_0 for the sample (●) without or (▼) with the cells. The inset shows a typical BFP image. Note that a dark cross in the image is the joints of four waveplates in the radial polarizer. (b) Model layer structure for analysis of the cell−electrode cleft gap distance. The gap distance d is defined as the sum of the water layer and adhesion protein thickness.

Cleft Gap Distance of HEK293 Cells. Although the results prove that LISPM is a powerful technique to observe an overall cell−substrate interface instantaneously, the detailed cellular structure at the interface and quantitative measurement of the gap distance are difficult because of the propagation property of SPPs and inhomogeneous illumination. Therefore, here, SLSPM is used to measure the cleft gap distance of HEK293 cells. In this set of experiments, the cells are cultured on four different gold surfaces—PLL, laminin (LAM), and fibronectin (FIB) and bare—for 3−6 DIV, in which the cell density was kept the same for all samples. PLL- and FIB-coated substrates are known to result in good cell adhesion, while LAM-coated and bare substrates are the control. In SLSPM, the reflectivity spectrum as a function of in-plane wavenumber $k_{//}$ is obtained by measuring the reflected light intensity at the BFP along the radial direction. In a BFP image, SPR appears as a dark ring (the inset in Figure 3a) and its radius represents SPR propagation constant (*i.e.*, $k_{//} = k_{SP}$). In order to characterize layer properties including the cell−gold cleft gap distance d, those spectra were fitted by the Fresnel equations based on a model layer structure depicted in Figure 3b. In the model, the thicknesses or the refractive indices of titanium, gold, glass substrate, and cellular plasma membrane were assumed as t_{Ti} = 8 nm and n_{Ti} = 2.153 + 2.923i,[39] t_{Au} = 50 nm, n_{gl} = 1.78, t_{pm} = 7.5 nm, and n_{pm} = 1.5,[40] respectively. The refractive indices of gold layers n_{Au} were determined at the respective scanning areas with SLSPM. The adhesion protein thicknesses t_{ap} were measured after their deposition from the propagation constant shift of SPR. As a result, those for PLL, LAM, and FIB were determined as t_{ap} = 0.3 ± 0.1 (n_{ap} = 1.52,[41] a refractive index of bulk PLL), 2.9 ± 0.5 (n_{ap} = 1.45), and 3.1 ± 1.4 nm (n_{ap} = 1.45), respectively. When the cells were on the substrate, as seen in Figure 3a, the wavenumber equaling the total internal reflection angle shifted due to the higher refractive index of cellular cytoplasm with

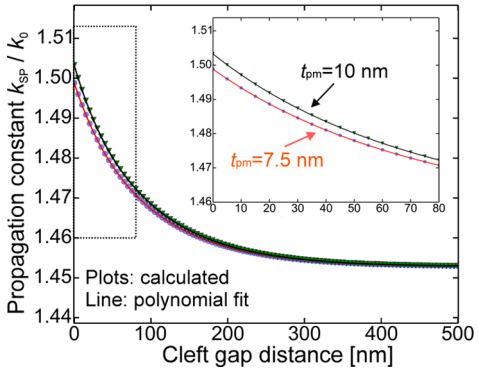

Figure 4. Calculated SPR propagation constant as a function of the gap distance at different thickness of plasma membrane (●: t_{pm} = 7.5 nm or ▼: t_{pm} = 10 nm). The inset is a magnified figure indicated with a dotted line square. The line indicates the eighth-order polynomial fitting curve. These plots are calculated with the experimentally obtained and assumed parameters.

respect to that of water.[42,43] They were found out to be n_{cp} = 1.361 ± 0.005 and n_{H_2O} = 1.335 ± 0.003 with SLSPM.

To determine the gap distance, the relationship between the distance and propagation constant of SPR was calculated upon the experimentally obtained and assumed optical constants. This was done by fitting the calculated propagation constants of SPR at the varied gap distances with an eighth degree polynomial function. The fitted function—the transfer function—can directly relate the distance to the propagation constant of SPR. The cleft gap distance was mapped in two dimensions by applying the transfer function to the propagation constant taken from the BFP at each scanning point. In Figure 4, the transfer function with the thickness of plasma membrane t_{pm} = 7.5 nm is presented. The plots were calculated with the refractive index of gold layer of a sample shown in Figure 5 (n_{Au} = 0.244 + 3.52i) and resulted in the function: $k_{SP}/k_0 = 1.49882 - 5.88039 \times 10^{-4} \times d + 4.48817 \times 10^{-6} \times d^2 - 2.61476 \times 10^{-8} \times d^3 +$

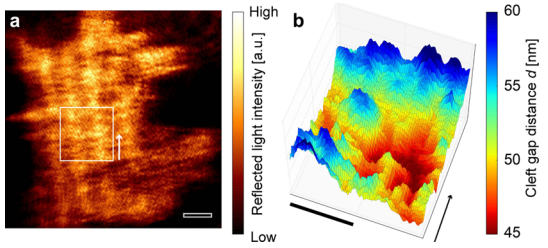

Figure 5. Representative (a) LISPM and (b) SLSPM images of HEK293 cells grown on PLL-coated gold surface. Scale bars are 5 μm. The square drawn in the LISPM image indicates the scanned area with SLSPM with the arrows indicating the orientation. Note that the brightness in LISPM image is tuned so as to enhance the contrast.

$1.12235 \times 10^{-10} \times d^4 - 3.26122 \times 10^{-13} \times d^5 + 5.93054 \times 10^{-16} \times d^6 - 6.03796 \times 10^{-19} \times d^7 + 2.61603 \times 10^{-22} \times d^8$ ($R^2 = 0.999999$). The propagation constant drastically changes until the gap distance reaches 200 nm. It is attributed to penetration depth of SPPs out of which they are not sensitive to a refractive index change anymore. Since a small variation in the propagation constants within 200 nm causes a huge error in the distance determination, we evaluated homogeneity of a gold film by measuring the propagation constant of a bare gold film over the area of 10×10 μm^2 in water, as shown in Supporting Information Figure S1. SLSPM revealed that the average propagation constant was of 1.451476 with a standard deviation of 0.000534, which is approximately 0.037%. This deviation corresponds to the error of 0.9 nm at the distance of 0 nm, where a change in the distance is the most drastic. Based on this result, we conclude that an error in the distance caused by a gold film is negligible, and its transfer function can be applied to any points in a respective scanned area. Besides, we also considered the error caused by a variation in the thickness of plasma membrane t_{pm} because it makes measurement of the distance difficult for interference methods.[7] In Figure 4, the plots at $t_{pm} = 10$ nm are shown. The deviation from the plots at $t_{pm} = 7.5$ nm reaches to the maximum of about 7 nm at the distance close to 0 nm and becomes small as the distance increases. It represents another advantage of SPM with which one can measure the distance (*i.e.*, the thickness of water) more precisely even though the thickness of plasma membrane is varied in a scanned area.

In order to validate our approach, measurement of the gap distance for HEK293 cells on PLL-coated gold surfaces for 3–6 DIV was demonstrated. In Figure 5, typical images taken with LISPM and SLSPM for the cell are presented. Owing to the capability of LISPM in simultaneous observation of a whole cell–gold interface, the image unveils the stretched shape of the cell bottom membrane on the gold, implying good adhesion with assistance of PLL. In the image, as seen in Figure 5a, stripe patterns attributed to the interference

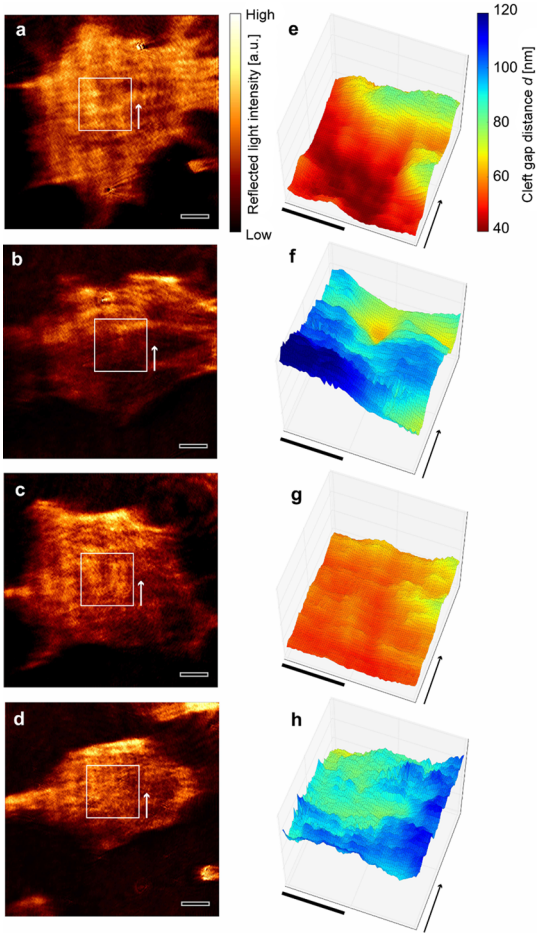

Figure 6. Images of HEK293 cells grown on (a,e) PLL, (b,f) LAM, and (c,g) FIB-coated, and (d,h) bare surfaces taken with LISPM (left column, a–d) and SLSPM (right column, e–h). Note that the brightness in LISPM images is tuned so as to enhance the contrast. Squares in LISPM images indicate the scanned areas with SLSPM with the arrows indicating the orientation. Scale bars are 5 μm.

of the light smears the detailed information, and thus quantitative evaluation of the gap distance is difficult with LISPM. In contrast, with SLSPM, the scanned image shown in Figure 5b well represents the cell–gold interface due to the high spatial resolution up to the diffraction limit.[35] The image revealed inhomogeneous gap distance distribution. After analysis and calculations, as previously mentioned, the cleft gap distances are determined, ranging from about 40 to 60 nm. The average distance eventually obtained from Figure 5b is 51.6 nm, which is in good agreement with the previously measured value (37 nm) with TEM.[13] The result supports our conclusion that our approach is effective for the gap distance measurement.

The cleft gap distances are also measured for the cells on LAM- and FIB-coated and bare gold surfaces in addition to the PLL-coated. The LISPM images presented in Figure 6a–d show details of the cell shape on each substrate. The cells on the PLL- and FIB-coated substrates show relatively stretched shape with respect to those on the LAM-coated and bare substrates.

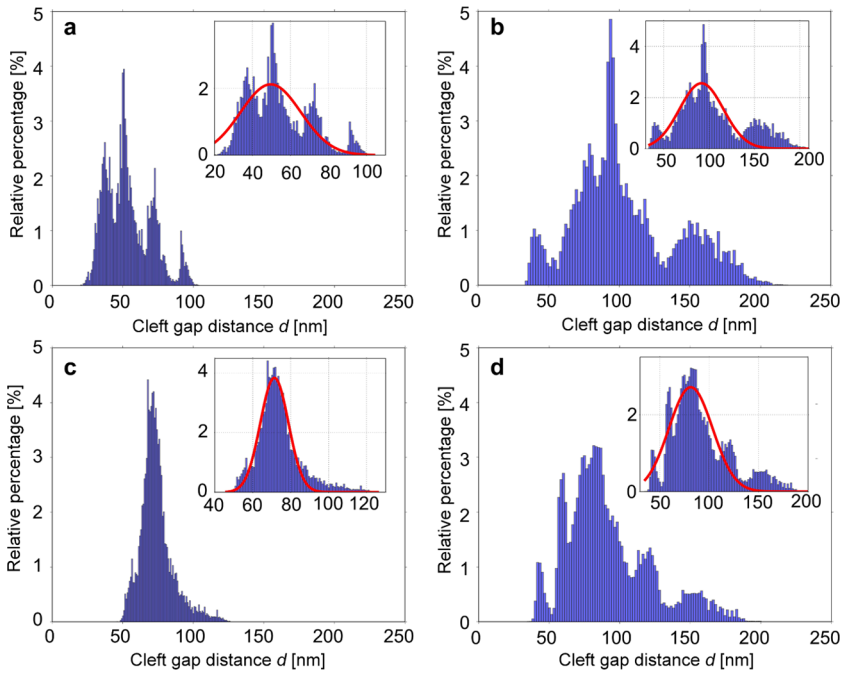

Figure 7. Comparison of the gap distances among four different surface coatings. (a) PLL, (b) LAM, (c) FIB, and (d) bare. Lines in the insets indicate Gaussian fits of the histograms.

However, quantitative comparison of the relative cellular adhesions among these different coatings is difficult because the incident angles of the excitation light are hardly known, thus the gap distances cannot be analytically determined. Then, the quantitative characterization of the gap distances was carried out with SLSPM, as shown in Figure 6e–h. First of all, it is clarified that the gap distances for the substrates coated with PLL and FIB are smaller than those for those coated with LAM and bare surface. This result supports our interpretation about the cellular adhesion in the LISPM images. Furthermore, the gap distance variations in each scanned area are recognizable in detail owing to the advantage of SLSPM.

The statistical analysis of the gap distance was conducted for a cumulative distance distribution histogram from $n = 12$ cells on each coating (Figure 7). We obtained the average gap distance by fitting the data with Gaussians (red curves in the insets in Figure 7), resulting in 49.6 ± 15.9 nm (PLL), 91.6 ± 24.2 nm (LAM), 71.4 ± 7.4 nm (FIB), and 81.3 ± 22.1 nm (bare). Compared to the simply averaged distances of 54.1 ± 16.3 nm (PLL), 107.0 ± 36.8 nm (LAM), 77.0 ± 11.7 nm (FIB), and 91.6 ± 30.3 nm (bare), it is found that the distances of the LAM and the bare differ more than those on the PLL and the FIB. It indicates that the distances on the LAM and the bare surface are more random because the cells adhere weakly on the surface, which could cause multiple peaks seen in Figure 7b,d. The multiple peaks seen in Figure 7a imply that the adhesion on the PLL is strong, but weak adhesion which could not be resolved with LISPM may also coexist. The distances of PLL and FIB are in excellent agreement with the previously reported 37 nm (PLL) with transmission electron microscopy[13] and 70 ± 10 nm and 75 ± 1 nm (FIB) with fluorescence interference contrast microscopy.[12,44] Among all the coatings, the PLL- and FIB-coated substrates show significantly and relatively small gap distances. In conjunction with the small statistical errors, we reach the same conclusion—good and homogeneous cellular adhesion—with that qualitatively obtained from the LISPM images (*e.g.*, Figure 2c). As is the case for the PLL- and FIB-coated substrates, the control samples—LAM-coated and bare substrates—show the large gap distances and statistical errors. These results represent poor and inhomogeneous cellular adhesions as interpreted from the LISPM images (*e.g.*, Figure 2d).

CONCLUSIONS

In summary, we demonstrate that the combined SPM is capable of the label-free and real-time observation of the cell–gold interface and measurement of its cleft gap distance with high spatial resolution. Simultaneous large area observation with LISPM allows one to visualize the cellular bottom membrane at the interface, which can be used for assessing the cellular adhesions qualitatively. The capability of real-time observation could be combined with experiments employing extra stimuli to cells. In addition, it enables one to select a region of interest to investigate in detail with SLSPM. By mapping the cleft gap distance quantitatively with SLSPM, the cellular adhesion differences among a variety of adhesion proteins and peptides are clarified. Furthermore, such morphological information as inhomogeneous gap distribution that cannot

be elucidated with LISPM is also revealed owing to the high spatial resolution of SLSPM. These presented abilities achieved without any labeling simplify an analysis of biointerface and the cell–electrode cleft gap distance.

METHODS

Sample Preparation. For SPP excitation, sapphire glass coverslips (Olympus) were coated with an 8 nm adhesion layer of titanium, followed by 50 nm of gold. The roughness of the gold surface of 0.88 ± 0.08 nm was measured with atomic force microscopy. Afterward, the substrate was sterilized under UV light exposure for 1 h. After sterilization, the substrates were coated with different adhesion peptides or proteins—PLL, LAM, and FIB—for 1 h at room temperature: for PLL, 10 $\mu g \cdot mL^{-1}$ and LAM 5 $\mu g \cdot mL^{-1}$ in Hanks' balanced salt solution (HBSS), and for FIB, 12.5 $\mu g \cdot mL^{-1}$ in phosphate buffered saline (PBS). As a control, the substrate without protein coating was also prepared.

Cell Culture. HEK293 cells were grown in Dulbecco's modified eagle medium and supplemented with 2 mM glutamine, 1% nonessential amino acids, 10% fetal bovine serum, 100 units $\cdot mL^{-1}$ K1 penicillin, and 0.1 mg $\cdot mL^{-1}$ K1 streptomycin (all from Invitrogen). The cells were plated on the substrate and cultured for 3–6 DIV at 37 °C and 5% CO_2. The cellular densities were 75 cells $\cdot mm^{-2}$ in all samples.

Optical Setup. The optical setup combining LISPM and SLSPM is shown in Figure S1 Supporting Information. The microscope can be switched by two flipping mirrors, FM1 and FM2. In SLSPM, a 10 mW HeNe laser (λ = 632.8 nm, Melles Griot) expanded after the beam expander (BE) converts its polarization from linear to quasi-radial with ZPol (nanophoton, Japan). The light after ZPol is relayed onto the BFP of a 100× 1.65 numerical aperture oil objective (OBJ, Olympus) by telecentric imaging system with two lenses (L1 and L2). The reflected light is imaged onto a CMOS camera (CMOS1, XIMEA) by a lens (L3). While scanning, the sample stage is moved by a piezo stage (Physik Instrumente) in *x* and *y* directions. In LISPM, the expanded beam after BE is focused on BFP with a lens (L4), which results in a plane wave incident to the substrate at a given incident angle. The reflected light is imaged by a lens (L5) on another CMOS camera (CMOS2, XIMEA).

Conflict of Interest: The authors declare no competing financial interest.

Acknowledgment. K.T. acknowledges the support provided by the Alexander von Humboldt Foundation.

Supporting Information Available: SPR propagation constant of a bare gold film in water measured with SLSPM. This material is available free of charge *via* the Internet at http://pubs.acs.org.

REFERENCES AND NOTES

1. Spira, M. E.; Hai, A. Multi-electrode Array Technologies for Neuroscience and Cardiology. *Nat. Nanotechnol.* **2013**, *8*, 83–94.
2. Kleinfeld, D.; Kahler, K.; Hockberger, P. Controlled Outgrowth of Dissociated Neurons on Patterned Substrates. *J. Neurosci.* **1988**, *8*, 4098–4120.
3. Sorribas, H.; Braun, D.; Leder, L.; Sonderegger, P.; Tiefenauer, L. Adhesion Proteins for a Tight Neuron–Electrode Contact. *J. Neurosci. Methods* **2001**, *104*, 133–141.
4. Brüggemann, D.; Wolfrum, B.; Maybeck, V.; Mourzina, Y.; Jansen, M.; Offenhäusser, A. Nanostructured Gold Microelectrodes for Extracellular Recording from Electrogenic Cells. *Nanotechnology* **2011**, *22*, 265104.
5. Hai, A.; Shappir, J.; Spira, M. E. In-Cell Recordings by Extracellular Microelectrodes. *Nat. Methods* **2010**, *7*, 200–202.
6. Wesche, M.; Hüske, M.; Yakushenko, A.; Brüggemann, D.; Mayer, D.; Offenhäusser, A.; Wolfrum, B. A Nanoporous Alumina Microelectrode Array for Functional Cell-Chip Coupling. *Nanotechnology* **2012**, *23*, 495303.
7. Limozin, L.; Sengupta, K. Quantitative Reflection Interference Contrast Microscopy (RICM) in Soft Matter and Cell Adhesion. *ChemPhysChem* **2009**, *10*, 2752–2768.
8. Barr, V. A.; Bunnell, S. C. Interference Reflection Microscopy. *Curr. Protoc. Cell Biol.* **2009**, *UNIT 4.23*, 1–21.
9. Axelrod, D. Cell–Substrate Contacts Illuminated by Total Internal Reflection Fluorescence. *J. Cell Biol.* **1981**, *89*, 141–145.
10. Braun, D.; Fromherz, P. Fluorescence Interference-Contrast Microscopy of Cell Adhesion on Oxidized Silicon. *Appl. Phys. A: Mater. Sci. Process.* **1997**, *348*, 341–348.
11. Braun, D.; Fromherz, P. Fluorescence Interferometry of Neuronal Cell Adhesion on Microstructured Silicon. *Phys. Rev. Lett.* **1998**, *81*, 5241–5244.
12. Gleixner, R.; Fromherz, P. The Extracellular Electrical Resistivity in Cell Adhesion. *Biophys. J.* **2006**, *90*, 2600–2611.
13. Wrobel, G.; Höller, M.; Ingebrandt, S.; Dieluweit, S.; Sommerhage, F.; Bochem, H. P.; Offenhäusser, A. Transmission Electron Microscopy Study of the Cell–Sensor Interface. *J. R. Soc. Interface* **2008**, *5*, 213–222.
14. Lin, Z. C.; Xie, C.; Osakada, Y.; Cui, Y.; Cui, B. Iridium Oxide Nanotube Electrodes for Sensitive and Prolonged Intracellular Measurement of Action Potentials. *Nat. Commun.* **2014**, *5*, 3206.
15. Fendyur, A.; Mazurski, N.; Shappir, J.; Spira, M. E. Formation of Essential Ultrastructural Interface between Cultured Hippocampal Cells and Gold Mushroom-Shaped MEA—Toward "IN-CELL" Recordings from Vertebrate Neurons. *Front. Neuroeng.* **2011**, *4*, 14.
16. Hanson, L.; Lin, Z. C.; Xie, C.; Cui, Y.; Cui, B. Characterization of the Cell–Nanopillar Interface by Transmission Electron Microscopy. *Nano Lett.* **2012**, *12*, 5815–5820.
17. Santoro, F.; Schnitker, J.; Panaitov, G.; Offenhäusser, A. On Chip Guidance and Recording of Cardiomyocytes with 3D Mushroom-Shaped Electrodes. *Nano Lett.* **2013**, *13*, 5379–5384.
18. Py, C.; Salim, D.; Monette, R.; Comas, T.; Fraser, J.; Martinez, D.; Martina, M.; Mealing, G. Cell to Aperture Interaction in Patch-Clamp Chips Visualized by Fluorescence Microscopy and Focused-Ion Beam Sections. *Biotechnol. Bioeng.* **2011**, *108*, 1936–1941.
19. Wierzbicki, R.; Køber, C.; Jensen, M. R. B.; Lopacińska, J.; Schmidt, M. S.; Skolimowski, M.; Abeille, F.; Qvortrup, K.; Mølhave, K. Mapping the Complex Morphology of Cell Interactions with Nanowire Substrates Using FIB-SEM. *PLoS One* **2013**, *8*, e53307.
20. Xie, C.; Lin, Z.; Hanson, L.; Cui, Y.; Cui, B. Intracellular Recording of Action Potentials by Nanopillar Electroporation. *Nat. Nanotechnol.* **2012**, *7*, 185–190.
21. Chizhik, A. I.; Rother, J.; Gregor, I.; Janshoff, A.; Enderlein, J. Metal-Induced Energy Transfer for Live Cell Nanoscopy. *Nat. Photonics* **2014**, *8*, 124–127.
22. Rothenhäusler, B.; Knoll, W. Surface Plasmon Microscopy. *Nature* **1988**, *332*, 615–617.
23. Hickel, W.; Kamp, D.; Knoll, W. Surface-Plasmon Microscopy. *Nature* **1989**, *339*, 186.
24. Hickel, W.; Knoll, W. Time- and Spatially Resolved Surface Plasmon Optical Investigation of the Photodesorption of Langmuir–Blodgett Multilayer Assemblies. *Thin Solid Films* **1991**, *199*, 367–373.
25. Giebel, K.-F.; Bechinger, C.; Herminghaus, S.; Riedel, M.; Leiderer, P.; Weiland, U.; Bastmeyer, M. Imaging of Cell/Substrate Contacts of Living Cells with Surface Plasmon Resonance Microscopy. *Biophys. J.* **1999**, *76*, 509–516.
26. Shinohara, H.; Sakai, Y.; Mir, T. A. Real-Time Monitoring of Intracellular Signal Transduction in PC12 Cells by Two-Dimensional Surface Plasmon Resonance Imager. *Anal. Biochem.* **2013**, *441*, 185–189.

27. Wang, W.; Wang, S.; Liu, Q.; Wu, J.; Tao, N. Mapping Single-Cell−Substrate Interactions by Surface Plasmon Resonance Microscopy. *Langmuir* **2012**, *28*, 13373–13379.
28. Wang, W.; Yang, Y.; Wang, S.; Nagaraj, V. J.; Liu, Q.; Wu, J.; Tao, N. Label-Free Measuring and Mapping of Binding Kinetics of Membrane Proteins in Single Living Cells. *Nat. Chem.* **2012**, *4*, 846–853.
29. Stabler, G.; Somekh, M. G.; See, C. W. High-Resolution Wide-Field Surface Plasmon Microscopy. *J. Microsc.* **2004**, *214*, 328–333.
30. Somekh, M. G. M.; Stabler, G.; Liu, S.; Zhang, J.; See, C. W. C. Wide-Field High-Resolution Surface-Plasmon Interference Microscopy. *Opt. Lett.* **2009**, *34*, 3110–3112.
31. Kano, H.; Mizuguchi, S.; Kawata, S. Excitation of Surface-Plasmon Polaritons by a Focused Laser Beam. *J. Opt. Soc. Am. B* **1998**, *15*, 1381–1386.
32. Kano, H.; Knoll, W. A Scanning Microscope Employing Localized Surface-Plasmon-Polaritons as a Sensing Probe. *Opt. Commun.* **2000**, *182*, 11–15.
33. Kano, H.; Knoll, W. Locally Excited Surface-Plasmon-Polaritons for Thickness Measurement of LBK Films. *Opt. Commun.* **1998**, *153*, 235–239.
34. Toma, M.; Knoll, W.; Dostalek, J. Bragg-Scattered Surface Plasmon Microscopy: Theoretical Study. *Plasmonics* **2011**, *7*, 293–299.
35. Watanabe, K.; Horiguchi, N.; Kano, H. Optimized Measurement Probe of the Localized Surface Plasmon Microscope by Using Radially Polarized Illumination. *Appl. Opt.* **2007**, *46*, 4985–4990.
36. Huang, B.; Yu, F.; Zare, R. N. Surface Plasmon Resonance Imaging Using a High Numerical Aperture Microscope Objective. *Anal. Chem.* **2007**, *79*, 2979–2983.
37. Halpern, A. R.; Wood, J. B.; Wang, Y.; Corn, R. M. Surface Plasmon Resonance Microscopy for Real-Time Measurements of DNA Hybridization Adsorption. *ACS Nano* **2014**, *8*, 1022–1030.
38. Watanabe, K.; Matsuura, K.; Kawata, F.; Nagata, K.; Ning, J.; Kano, H. Scanning and Non-scanning Surface Plasmon Microscopy To Observe Cell Adhesion Sites. *Biomed. Opt. Express* **2012**, *3*, 354–359.
39. Lynch, D. W.; Olson, C. G.; Weaver, J. H. Optical Properties of Ti, Zr, and Hf from 0.15 to 30 eV. *Phys. Rev. B* **1975**, *11*, 3617–3624.
40. Meyer, R. A. Light Scattering from Biological Cells: Dependence of Backscatter Radiation on Membrane Thickness and Refractive Index. *Appl. Opt.* **1979**, *18*, 585–588.
41. Luckham, P.; Klein, J. Forces between Mica Surfaces Bearing Adsorbed Polyelectrolyte, Poly-L-Lysine, in Aqueous Media. *J. Chem. Soc., Faraday Trans.* **1984**, *80*, 865–878.
42. Schmitt, J. M.; Kumar, G. Optical Scattering Properties of Soft Tissue: A Discrete Particle Model. *Appl. Opt.* **1998**, *37*, 2788–2797.
43. Brunsting, A.; Mullaney, P. F. Differential Light Scattering from Spherical Mammalian Cells. *Biophys. J.* **1974**, *14*, 439–453.
44. Brittinger, M.; Fromherz, P. Field-Effect Transistor with Recombinant Potassium Channels: Fast and Slow Response by Electrical and Chemical Interactions. *Appl. Phys. A: Mater. Sci. Process.* **2005**, *81*, 439–447.